

Intra-granular fission gas bubbles growth in crystalline U_3Si_2: Rate theory modeling

Cong Ma(马聪), Youheng Pei(裴有恒), Tianyuan Xin(信天缘), Dmitrii O. Kharchenko, Vasyl O. Kharchenko, Baoqin Fu(付宝勤), Qing Hou(侯氢), Changqing Teng(滕常青), and Lu Wu(吴璐)
Citation: Chin. Phys. B, 2025, 34 (**12**): 126101. DOI: 10.1088/1674-1056/ade42b
http://cpb.iphy.ac.cn; http://iopscience.iop.org/cpb

What follows is a list of articles you may be interested in

High-burn-up structure evolution in polycrystalline UO_2: Phase-field modeling investigation

Dan Sun(孙丹), Yanbo Jiang(姜彦博), Chuanbao Tang(唐传宝), Yong Xin(辛勇), Zhipeng Sun(孙志鹏), Wenbo Liu(柳文波), and Yuanming Li(李垣明)
Chin. Phys. B, 2025, 34 (**2**): 026102. DOI: 10.1088/1674-1056/ad9c42

Effect of grain size on gas bubble evolution in nuclear fuel: Phase-field investigations

Dan Sun(孙丹), Qingfeng Yang(杨青峰), Jiajun Zhao(赵家珺), Shixin Gao(高士鑫), Yong Xin(辛勇), Yi Zhou(周毅), Chunyu Yin(尹春雨), Ping Chen(陈平), Jijun Zhao(赵纪军), and Yuanyuan Wang(王园园)
Chin. Phys. B, 2024, 33 (**1**): 016105. DOI: 10.1088/1674-1056/ad08a6

Application of silicon carbide temperature monitors in 49-2 swimming-pool test reactor

Guang-Sheng Ning(宁广胜), Li-Min Zhang(张利民), Wei-Hua Zhong(钟巍华), Sheng-Hong Wang(王绳鸿), Xin-Yu Liu(刘心语), Ding-Ping Wang(汪定平), An-Ping He(何安平), Jian Liu(刘健), and Chang-Yi Zhang(张长义)
Chin. Phys. B, 2023, 32 (**5**): 056102. DOI: 10.1088/1674-1056/acb41c

Atomic simulations of primary irradiation damage in U-Mo-Xe system

Wen-Hong Ouyang(欧阳文泓), Jian-Bo Liu(刘剑波), Wen-Sheng Lai(赖文生),Jia-Hao Li(李家好), and Bai-Xin Liu(柳百新)
Chin. Phys. B, 2023, 32 (**3**): 036101. DOI: 10.1088/1674-1056/ac9366

Helium bubble formation and evolution in NiMo-Y_2O_3 alloy under He ion irradiation

Awen Liu(刘阿文), Hefei Huang(黄鹤飞), Jizhao Liu(刘继召), Zhenbo Zhu(朱振博), and Yan Li(李燕)
Chin. Phys. B, 2022, 31 (**4**): 046102. DOI: 10.1088/1674-1056/ac3654

Intra-granular fission gas bubbles growth in crystalline U_3Si_2: Rate theory modeling

Cong Ma(马聪)[1,2,3], Youheng Pei(裴有恒)[2,4], Tianyuan Xin(信天缘)[2,3], Dmitrii O. Kharchenko[5], Vasyl O. Kharchenko[5,6], Baoqin Fu(付宝勤)[1], Qing Hou(侯氢)[1], Changqing Teng(滕常青)[2], and Lu Wu(吴璐)[2,3,†]

[1] *Institute of Nuclear Science and Technology, Sichuan University, Chengdu* 610064, *China*
[2] *The First Sub-Institute, Nuclear Power Institute of China, Chengdu* 610213, *China*
[3] *National Key Laboratory of Nuclear Reactor Technology, Nuclear Power Institute of China, Chengdu* 610213, *China*
[4] *Department of Engineering Physics, Tsinghua University, Beijing* 100084, *China*
[5] *Institute of Applied Physics, National Academy of Sciences of Ukraine*, 58 *Petropavlivska St.*, 40000 *Sumy, Ukraine*
[6] *Sumy State University*, 116 *Kharkivska St.*, 40007 *Sumy, Ukraine*

(Received 22 April 2025; revised manuscript received 30 May 2025; accepted manuscript online 13 June 2025)

A model of intra-grain fission gas bubble growth in U_3Si_2 coupled with defect microstructure is generalized to take into account the influence of point defect sinks and defect clustering. The dynamics of bubble growth and defect structure properties are studied under different irradiation conditions. The influence of temperature and flux on bubble growth, defect ensemble evolution, and changes in material properties (elastic moduli and thermal degradation factor) are examined in detail. The universality of the bubble size distribution and the crossover of dynamical regimes of bubble growth are studied under various irradiation conditions. It is shown that a change in the dominant (fission gas atom- or vacancy-mediated) mechanism of bubble growth results in a crossover from a parabolic to a sub-parabolic bubble size growth law. The proposed modification of the rate theory model provides more accurate predictions and more detailed insight into fuel performance, especially fission gas behavior in crystalline U_3Si_2.

Keywords: U_3Si_2, gas bubbles, swelling, elastic and thermal properties

PACS: 61.80.Az, 61.72.J–, 61.72.–y

DOI: 10.1088/1674-1056/ade42b **CSTR:** 32038.14.CPB.ade42b

1. Introduction

Challenges to enhancing both the safety and performance of light water reactors (LWRs) have remained an active area of research in recent years (see Ref. [1] and citations therein). U_3Si_2 is considered a promising alternative to UO_2 as an accident-tolerant fuel for commercial LWRs. Its higher thermal conductivity compared to UO_2 implies a reduction in stored thermal energy within the fuel, which is a critical factor during loss of coolant accidents (LOCA).[2–4] These exceptional properties lead to reduced thermal energy storage and lower enrichment requirements, positioning U_3Si_2 as a material with excellent accident tolerance. Additionally, it offers advantages for the fuel cycle, such as decreased enrichment needs and the potential for extended fuel life. Consequently, U_3Si_2 is considered a highly promising candidate for accident-tolerant fuel. Several advantages of U_3Si_2 compared to UO_2, especially regarding its swelling behavior, remain under active discussion.[5,6]

The performance of U_3Si_2 fuel under research reactor conditions has been thoroughly studied.[1,7–11] In research reactors, where typical fuel temperatures are below 523 K, U_3Si_2 becomes amorphized by irradiation at as low as 0.3 dpa, meaning it loses crystallinity within the first days of reactor operation. Fission-induced amorphization, which affects swelling, can be suppressed at the higher operating temperatures typical of LWRs, where U_3Si_2 temperature remains well above 523 K and the crystalline phase is retained. The scarcity of experimental data on gas bubble growth and swelling under LWR conditions motivates the development of theoretical models and simulation codes to predict fuel performance at elevated temperatures. For example, GRASS-SST simulations have been employed to study fission gas behavior in LWRs and in comparison to conventional oxide LWR fuels.[12] It was noted that these studies heavily rely on experimental data from reactors.[13] Fission gas behavior under various LOCA conditions (temperatures from 600 K to 1600 K) in LWRs was simulated using rate theory (GRASS-SST code) coupled with thermomechanics (BISON code[14]). It was shown that at $T < 1000$ K, swelling is mainly due to intragranular bubbles, whereas at elevated temperatures, grain boundary bubbles form and become the primary contributors to swelling. Further temperature increases lead to interconnection of intragranular bubbles, formation of gas release channels, and a dramatic reduction in swelling. According to these simulation

†Corresponding author. E-mail: wulu1002@qq.com

© 2025 Chinese Physical Society and IOP Publishing Ltd. All rights, including for text and data mining, AI training, and similar technologies, are reserved.

results, under normal LWR conditions, the overwhelming majority of fission gas is retained in intragranular bubbles.[15]

In the crystalline phase, bubbles consist of both fission gas atoms and vacancies.[16] This leads to an increase in fuel porosity, causing macroscopic effects such as gas swelling, reduction in thermal conductivity,[17] and changes in elastic moduli.[5] Analysis of bubble size distributions from GRASS-SST simulations showed that small intragranular bubbles saturate at a size of about 1.5 nm, with their number density increasing with burnup. Larger intragranular bubbles with sizes $R_b > 2$ nm, which emerge at elevated temperatures due to enhanced fission gas (Xe) diffusion, saturate in number density at approximately 2×10^{22} m^{-3}. However, their size continues to grow with burnup, resulting in swelling up to 5% at temperatures up to 900 K.[15] When considering bubble growth in crystalline systems at intermediate temperatures (600 K $< T <$ 900 K), it is important to account for evolving sinks such as dislocations, dislocation loops, and grain boundaries. These sinks cause the formation of cellular dislocation structures that transform into subgrains,[18] thereby affecting bubble distribution and resulting in local variations of macroscopic fuel properties inside grains.

In this paper, we aim to study changes in the characteristics of ensembles of both bubbles and defects. We generalize previous rate theory models for U_3Si_2 under LWR conditions[19] by incorporating point defect and gas atom sinks, which influence the absorption of gas atoms from the matrix and govern bubble growth rates. We discuss thermal and flux effects at moderate temperatures. It will be shown that the bubble size distribution exhibits universal features characterized by heavy tails. Our study considers the so-called automodel regime, enabling time-dependent bubble size distribution functions and direct derivation of scaling laws for mean bubble size. We demonstrate that the scaling dynamics manifest a crossover between dynamical regimes governing bubble growth.

The paper is organized as follows. In Section 2, we briefly describe the model and introduce modifications to the rate theory model related to defect clustering, cellular dislocation structures, and dislocation loop growth inside grains. Section 3 discusses the main results of the rate theory modeling. Here, we analyze data obtained under different conditions and consider the dynamics of both mean bubble size and mean dislocation loop size at various irradiation scenarios. At the end of this section, we propose a procedure to obtain the universal bubble size distribution and scaling asymptotics for bubble growth. It will be shown that the crossover between dynamical regimes of bubble growth is related to competition between two governing mechanisms: fission gas atom accumulation versus vacancy accumulation. Conclusions are presented in Section 4.

2. Main governing equations

When considering gas bubble growth in a crystalline system, one must account for point defects, their sinks, and gas atoms (Xe). In the following mathematical model, we include evolving point defect sinks such as network dislocations, dislocation loops, and gas bubbles, as well as stationary sinks related to grain boundaries. Experimental evidence shows that gas atoms can migrate to grain boundaries and dislocations.[20] We assume that network dislocations can form a cellular dislocation structure, which limits the growth of dislocation loops and influences the dynamics of bubble growth.[18,21,22]

Following the approach developed in Ref. [23], the dynamics of interstitial and vacancy concentrations (c_i, c_v) are described by the equations

$$\begin{aligned}
\partial_t c_i &= K - k_i^2 D_i c_i - \alpha_r c_i c_v - \frac{\sqrt{2}}{\Omega_0^{2/3}} D_i c_i^2 \\
&\quad + \frac{\Omega_0^{1/3} b_v D_v}{\pi} \frac{N_L c_v}{R_L}, \\
\partial_t c_v &= K - k_v^2 D_v c_v - \alpha_r c_i c_v \\
&\quad - \frac{\Omega_0^{1/3} b_v D_v}{\pi} \frac{N_L c_v}{R_L} + K_{em}^b.
\end{aligned} \tag{1}$$

Here, K is the defect generation rate; D_i and D_v are the diffusivities of interstitials and vacancies, respectively; b_v is the modulus of the Burgers vector; and α_r is the recombination rate constant, defined in the standard way. The quantities N_L and R_L represent the number density and radius of interstitial dislocation loops. The atomic volume of uranium in U_3Si_2 is approximated by $\Omega_0 \simeq a^3$,[23] where a is the lattice constant.

The sink strength for $q = \{i, v\}$ point defects (interstitials i and vacancies v) is defined as

$$k_q^2 = Z_{Nq}\rho_N + Z_{Lq}\rho_L + Z_{bq}R_b N_b + Z_{GB}\lambda_{GB}^{-2}, \tag{2}$$

where Z_{Nq} is the preference factor for network dislocations with density ρ_N, Z_{Lq} relates to interstitial dislocation loops with density $\rho_L = 2\pi R_L N_L$, Z_{GB} corresponds to grain boundaries with characteristic radius λ_{GB}, and Z_{bq} describes the effect of bubbles with size R_b and number density N_b. The term $Z_{qb} = 4\pi Y_q$ accounts for the preference of q-type point defects being absorbed, where Y_q is the absorption preference factor.[25] Following Ref. [26] we use the values $Z_{Ni} = 1.1$, $Z_{Nv} = 1.0$, $Z_{Li} = 1.005$, $Z_{Lv} = 1.0$ and $Z_{GB} = 24$ and assume vacancy absorption preference $Y_v = 1.005$ and interstitial absorption preference $Y_i = 1.0$, reflecting the greater likelihood of vacancies being absorbed by bubbles. The last term K_{em}^b in the vacancy concentration equation represents vacancy emission from bubbles driven by bubble pressure differences, which will be defined later.

The evolution equations for dislocation loop number density and radius are given by[22]

$$\begin{aligned}\partial_t N_{\rm L} &= \frac{\sqrt{2}}{2}\frac{D_{\rm i}}{\Omega_0^{5/3}}c_{\rm i}^2 - \frac{4N_{\rm L}}{\pi R_{\rm L}}v_{\rm cl} - \frac{b_{\rm v}D_{\rm v}}{\pi\Omega_0^{2/3}}\frac{c_{\rm v}N_{\rm L}}{R_{\rm L}},\\ \partial_t R_{\rm L} &= g_{\rm L}\left(v_{\rm cl} - (R_{\rm L}-R_{\rm L}^0)\frac{\partial_t N_{\rm L}}{2N_{\rm L}} + \frac{K_{\rm i}\varepsilon_{\rm ig}(\pi r_{\rm icl})^2\tilde{\rho}}{2d_{\rm i}b_{\rm v}S_{\rm icl}}\right).\end{aligned} \quad (3)$$

Here, the climbing velocity is defined as $v_{\rm cl} = b_{\rm v}^{-1}(Z_{\rm Li}D_{\rm i}\bar{c}_{\rm i} - Z_{\rm Lv}D_{\rm v}\bar{c}_{\rm v})$ and $R_{\rm L}^0$ is the loop radius cutoff. The parameter $\varepsilon_{\rm ig}$ denotes the fraction of glissile interstitial clusters. The sink strength of defect clusters is given by Refs. [26,27]: $S_{\rm icl} = 2(\pi r_{\rm icl}\tilde{\rho}/2)^2$, where $\tilde{\rho} = \rho_{\rm N} + \rho_{\rm L} + \dfrac{2}{\pi r_{\rm icl}\lambda_{\rm GB}}$, $r_{\rm icl}$ is the capture radius for mobile interstitial clusters, and these clusters migrate along $d_{\rm i} = 3$ crystallographic directions (assumed equal). The cellular dislocation structure limits loop growth and is modeled through the factor:[22] $g_{\rm L} = C_{\rm A}C_\rho\sqrt{\pi/f(\nu)} - 2R_{\rm I}\sqrt{\tilde{\rho}}$, with $C_{\rm A}C_\rho = 2.185$,[28] $f(\nu) = \dfrac{1-\nu/2}{1-\nu}$ where ν is the Poisson ratio.

Network dislocation density can be both generated and relaxed. These dislocations form a cellular network structure, whose density $\rho_{\rm N}$ evolves according to[18]

$$\partial_t\rho_{\rm N} = v_{\rm cl}\left(2\pi N_{\rm L} - \frac{\rho_{\rm N}}{2\lambda_{\rm GB}} - \frac{\sqrt{f_v/\pi}}{C_{\rm A}C_\rho}\rho_{\rm N}^{3/2}\right). \quad (4)$$

The terms represent, respectively, creation of dislocation line length due to interstitial loop accumulation, loss due to capture by grain boundaries, and loss via self-annihilation from correlated dislocation motion.

Following Ref. [23], the dynamics of fission gas (Xe) concentration within grains ($c_{\rm g}$), bubble number density ($N_{\rm b}$), gas atom content ($m_{\rm b}$), and vacancy content ($n_{\rm vb}$) in bubbles of size $R_{\rm b}$ are described by

$$\begin{aligned}\partial_t c_{\rm g} &= K_{\rm g} - 16\pi f_{\rm n} r_{\rm g} D_{\rm g} c_{\rm g}^2 - k_{\rm g}^2 D_{\rm g} c_{\rm g} + 2bm_{\rm b}N_{\rm b},\\ \partial_t N_{\rm b} &= 16\pi f_{\rm n} r_{\rm g}\frac{D_{\rm g}c_{\rm g}^2}{m_{\rm b}} - bN_{\rm b} - 16\pi R_{\rm b}D_{\rm b}N_{\rm b}^2,\\ \partial_t m_{\rm b} &= 4\pi R_{\rm b}D_{\rm g}c_{\rm g} - bm_{\rm b} + 16\pi R_{\rm b}D_{\rm b}m_{\rm b}N_{\rm b},\\ \partial_t n_{\rm vb} &= (Z_{\rm bv}D_{\rm v}c_{\rm v} - Z_{\rm bi}D_{\rm i}c_{\rm i})\frac{R_{\rm b}}{\Omega_{\rm v}} + \frac{2\pi D_{\rm v}d}{k_{\rm B}T}(p - p_{\rm eq}).\end{aligned} \quad (5)$$

Here, $K_{\rm g} = \beta\dot{f}$ is the gas atom generation rate per fission rate $\dot{f}$, with β as the gas atom production per fission. The gas-atom resolution rate is $b = b_0\dot{f}$, $f_{\rm n}$ is the nucleation factor, and $r_{\rm g}$ is the gas atom radius. The gas-bubble diffusivity is: $D_{\rm b} = 3\Omega_0 D_{\rm g}/4\pi R_{\rm b}^3$, and the average distance between bubbles is $d = N_{\rm b}^{-1/3}$. The sink strength for gas atoms is $k_{\rm g}^2 = Z_{gN}\rho_{\rm N} + Z_{\rm GB}\lambda_{\rm GB}^{-2}$ assuming that gas atoms condense at dislocations and grain boundaries with the same preference factors as point defects ($Z_{\rm N} = Z_{i\rm N}$). The radiation-enhanced diffusion coefficient for gas atoms is[22] $D_{\rm g} = D_{\rm g}^0 + D_{\rm g}^{\rm RED}\dot{f}$, where $D_{\rm g}^0$ is the baseline diffusion coefficient and $D_{\rm g}^{\rm RED}$ accounts for radiation enhancement.

The equilibrium bubble pressure is given by $p_{\rm eq} = 2\gamma/R_{\rm b}$, where γ is the surface tension. The bubble pressure p follows the van der Waals equation of state,[29] with mechanical equilibrium expressed as $p = p_{\rm eq} - \sigma$, where σ is the hydrostatic stress in the bulk material.

The mean bubble radius is computed from the bubble volume: $V_{\rm b} = \Omega_{\rm g}m_{\rm b} + \Omega_{\rm v}n_{\rm vb}$ using $R_{\rm b} = (3V_{\rm b}/4\pi)^{1/3}$, where $\Omega_{\rm g}$ and $\Omega_{\rm v}$ are the volumes of a gas atom and a vacancy, respectively.[19]

The first terms in Eq. (5) correspond to gas production at rate $K_{\rm g}$, bubble nucleation, and growth by gas atom absorption. The second and third terms in the $c_{\rm g}$ equation describe gas clustering and annihilation at grain boundaries, while the fourth term accounts for gas resolution from bubbles. The decrease of $N_{\rm b}$ is due to gas atom resolution and bubble coalescence, and changes in $m_{\rm b}$ reflect gas atom loss by resolution and gain by bubble migration. Vacancy production within bubbles from pressure differences is governed by the second term in the $n_{\rm vb}$ equation, corresponding to vacancy emission with rate

$$K_{\rm em}^{\rm b} = \frac{2\pi\Omega_{\rm v}}{k_{\rm B}T}(p_{\rm eq} - p)\frac{d}{R_{\rm b}},$$

which appears in the vacancy concentration equation Eq. (1). When $p > p_{\rm eq}$, bubbles absorb vacancies from the matrix; otherwise, they emit vacancies.

Solving the coupled system Eqs. (1)–(5) enables the study of bubble characteristics and the associated macroscopic effect of gas bubble swelling coupled with the evolving defect structure under various irradiation conditions.

The growth of gas bubbles causes swelling and porosity, which affect material properties such as thermal conductivity and elastic moduli.[30] Porosity is defined as $\varpi = s_{\rm b}/(1+s_{\rm b})$, where $s_{\rm b} = 4\pi R_{\rm b}^3 N_{\rm b}/3$ is the fractional swelling due to bubbles.[31]

To estimate the degradation of thermal conductivity, we use the Maxwell–Eucken formula,[31] which fits experimental data and modifies conductivity by the factor

$$\varkappa = \frac{1-\varpi}{1+0.9\varpi}. \quad (6)$$

For the elastic moduli (Young's modulus E and shear modulus G, in unit GPa), we apply a model calibrated with experimental data[5]

$$E = -6.425\varpi + 142.68, \quad G = -2.901\varpi + 61.27. \quad (7)$$

Thus, using the evolution of $R_{\rm b}$ and $N_{\rm b}$, we can analyze the changes in material properties of U_3Si_2 under different irradiation regimes.

The material parameters used in the subsequent analysis of bubble growth in a crystalline environment are summarized in Table 1.

Table 1. Material parameters for U_3Si_2 used in simulations.

Parameter	Description	Value	Ref.
a	Lattice constant	7.3314×10^{-8} cm	[32]
Ω_0	Atomic volume	3.629×10^{-23} cm^3	[24]
Ω_v	Vacancy volume	4.09×10^{-23} cm^3	[33]
Ω_g	van der Waals gas atom volume	8.5×10^{-23} cm^3	[19]
r_{iv}	Defect recombination radius	8.25×10^{-7} cm	[22]
b_v	Burgers vector modulus	0.382 nm	[34]
f_n	Bubble nucleation factor	10^{-4}	[19]
β	Gas atoms produced per fission	0.25	[23]
r_g	Radius of diffusion gas atom	0.216×10^{-7} cm	[21]
b_0	Effective resolution volume	$2.8\times10^{-25}(5\times10^{-10}/R_b)^{0.23}$ m^3	[19]
D_g^0	Gas atoms diffusion coefficient	$5.91\times10^{-2}\,e^{-2.75eV/k_BT}$ cm^2/s	[19]
D_g^{RED}	Proportionality constant	1.0×10^{-32} cm^5	[16]
K	Defect production rate	$10K_ga^3$ s^{-1}	[24]
D_v	Vacancy diffusivity	D_g	[24]
D_i	Interstitial diffusivity	$2.5\times10D_v$	–
ν	Poisson ratio	0.31	[23]
λ_{GB}	Grain size	20×10^{-4} cm	[25]

3. Results and discussion

3.1. Protocols description

Typical results of the simulations at fixed temperature and fission rate are shown in Fig. 1.

From Fig. 1(a) it follows that point defect concentrations increase with fission density $F_d = \dot{f}t$ and at elevated F_d attain stationary values. The gas atoms concentration increases up to its maximal value and at elevated F_d decreases due to effect of gas atoms sinks and nucleation processes. The final stage of evolution of both defect and gas atom concentrations at fission densities around 5×10^{20} cm^{-3} corresponds to irradiation time $\approx$ 55 hours. With further irradiation bubbles formed due to nucleation of gas atoms start to grow in a size and their number density increases as it is seen from Fig. 1(b). It follows that the quantity N_b grows rapidly when bubbles are small (of the radius up to (3–4) nm) and manifests delayed growth for large bubbles of the radius $\approx$ (8–10) nm. During this stage initially formed bubbles start to accumulate vacancies. At late stage of bubble growth a ratio $m_b/n_{vb} < 1$. It means that the main mechanism governing a growth of large bubbles (of the radius $\approx$ 10 nm) belongs to vacancies accumulation. By considering defect microstructure evolution one finds that mean loop radius increases fast up to $\approx$ 2.5 nm comparing to growth of bubble of the same size and after the growth rate is much lower. The loop size is lower than the radius of the mean bubble at elevated fission densities. The same crossover of dynamical regimes is observed for loop number density and network dislocation density. It follows that a difference in values of ρ_N and ρ_L remains of the same order with fission density increases, $\rho_L/\rho_N \approx 10$. It should be noted that typical dynamics of bubble size and their density corresponds well to theoretical results shown in Ref. [19].

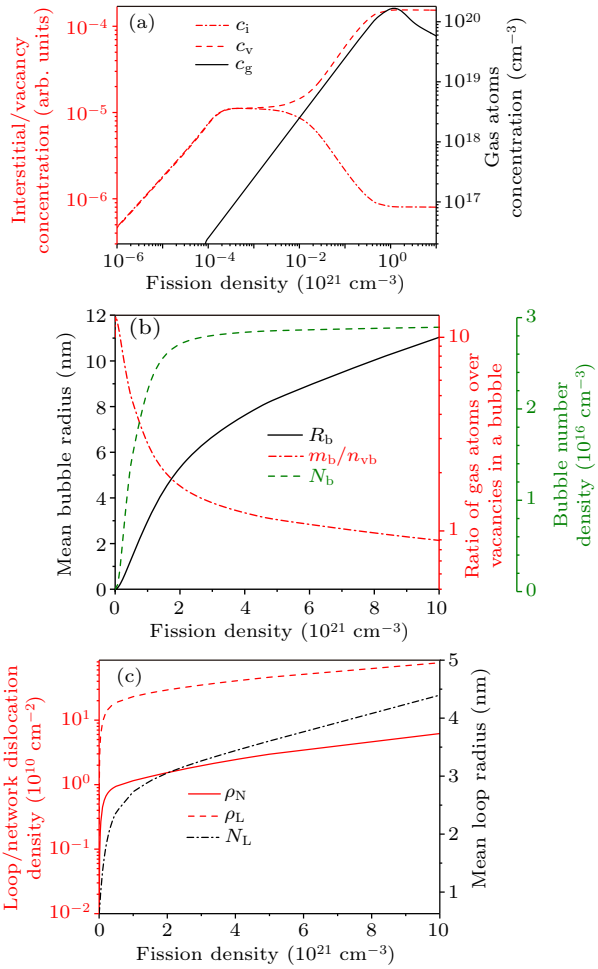


Fig. 1. Typical protocols obtained at T = 750 K, $\dot{f} = 2.5\times10^{14}$ (cm^3·s)$^{-1}$ for point defects and gas atoms concentrations (a), bubble radius, ratio of amount of gas atoms and vacancies in a bubble and bubble number density (b), loop radius and loop and network dislocation densities (c).

From Fig. 1(a), it is observed that point defect concentrations increase with fission density $F_d = \dot{f}t$ and eventually reach steady-state values at high F_d. The gas atom concentration ini-

tially rises to a maximum, then decreases at elevated F_d due to the effects of gas atom sinks and nucleation processes. The final stage of evolution for both defect and gas atom concentrations, occurring at fission densities around 5×10^{20} cm^{-3}, corresponds to an irradiation time of approximately 55 hours.

With continued irradiation, bubbles formed by gas atom nucleation begin to grow in size and their number density increases, as shown in Fig. 1(b). The bubble number density N_b increases rapidly when the bubbles are small (with radii up to approximately 3 nm–4 nm), and exhibits delayed growth for larger bubbles with radii around 8 nm–10 nm. During this stage, the initially formed bubbles start to accumulate vacancies. At later stages of bubble growth, the ratio $m_b/n_{vb} < 1$ indicates that vacancy accumulation becomes the dominant mechanism driving the growth of large bubbles (with radius near 10 nm).

Considering the evolution of the defect microstructure, the mean loop radius grows rapidly up to approximately 2.5 nm, which is smaller than the mean bubble radius at comparable fission densities. After this initial growth, the loop growth rate slows significantly. A similar crossover in dynamical regimes is observed for both loop number density and network dislocation density. The difference between ρ_N and ρ_L remains approximately constant as the fission density increases, with $\rho_L/\rho_N \approx 10$.

It should be noted that the typical dynamics of bubble size and number density are consistent with the theoretical results reported in Ref. [19].

3.2. Temperature effect

Next, let us consider the effects caused by variations in irradiation temperature. Protocols for the main measured quantities are shown in Fig. 2 for different irradiation temperatures.

From Fig. 2(a), it can be seen that the overall bubble growth dynamics remain unchanged; only the value of R_b increases with temperature. A significant difference in bubble size (on the order of 2 nm–3 nm at elevated F_d) is observed at temperatures above 800 K, whereas at lower temperatures this difference is approximately 1 nm. The bubble number density maintains its dynamic behavior but shows a decrease in magnitude with increasing temperature. Gas bubble swelling, computed in the standard manner as $S = s_b \times 100\%$ and shown in Fig. 2(b), exhibits an enhanced growth rate with increasing temperature. A crossover between dynamical regimes is observed at fission density values around 10^{21} cm^{-3}, where a slow increase transitions to rapid growth, corresponding to bubble radii around 3 nm and a change in the rate of bubble number density growth.

By comparing the dynamics of sinks for diffusing species shown in Fig. 2(c) at different temperatures, it is evident that at low temperatures (approximately 600 K), the network dislocation density ρ_N reaches a steady-state value, while the growth of loop density ρ_L remains delayed even at elevated fission densities. With increasing temperature, both ρ_N and ρ_L reach higher values. The increase in ρ_N is driven by the enhanced growth of loop number density N_L, whereas the more rapid growth of ρ_L relative to ρ_N is governed by increases in both the loop radius and loop number density N_L.

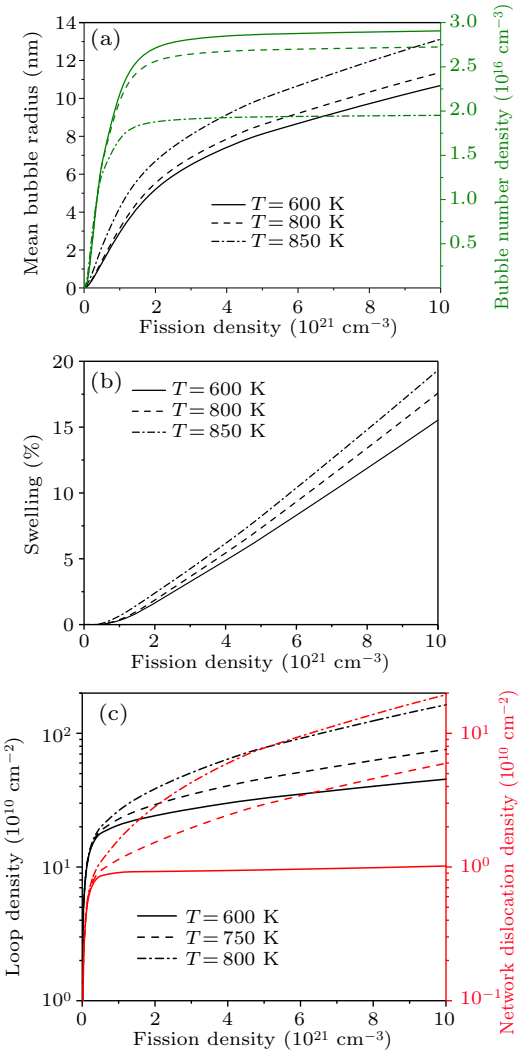


Fig. 2. Typical protocols for mean bubble radius and bubble number density (a), swelling (b), loop and network dislocation densities (c) at different temperatures at fixed fission rate $\dot{f} = 2.5 \times 10^{14}$ (cm^3·s)$^{-1}$.

A detailed analysis of the temperature effect can be performed by comparing the data for measured quantities at a fixed fission density $F_d = 3 \times 10^{21}$ cm^{-3}, corresponding to 3330 hours of irradiation, at different temperatures as shown in Fig. 3.

From Fig. 3(a), it follows that significant changes in bubble size, loop size, and dislocation cell size occur at elevated temperatures. Rapid growth is clearly observed for both bubble and loop sizes, whereas the dislocation cell size decreases sharply as temperature increases. Within the selected temperature range and fission density, the difference between cell size and loop size is approximately a factor of 10. This implies that at high temperatures, the recrystallization process will be governed by a combination of both line dislocations and dislocation loops, leading to a recrystallization scenario characterized by the formation of new sub-grains.

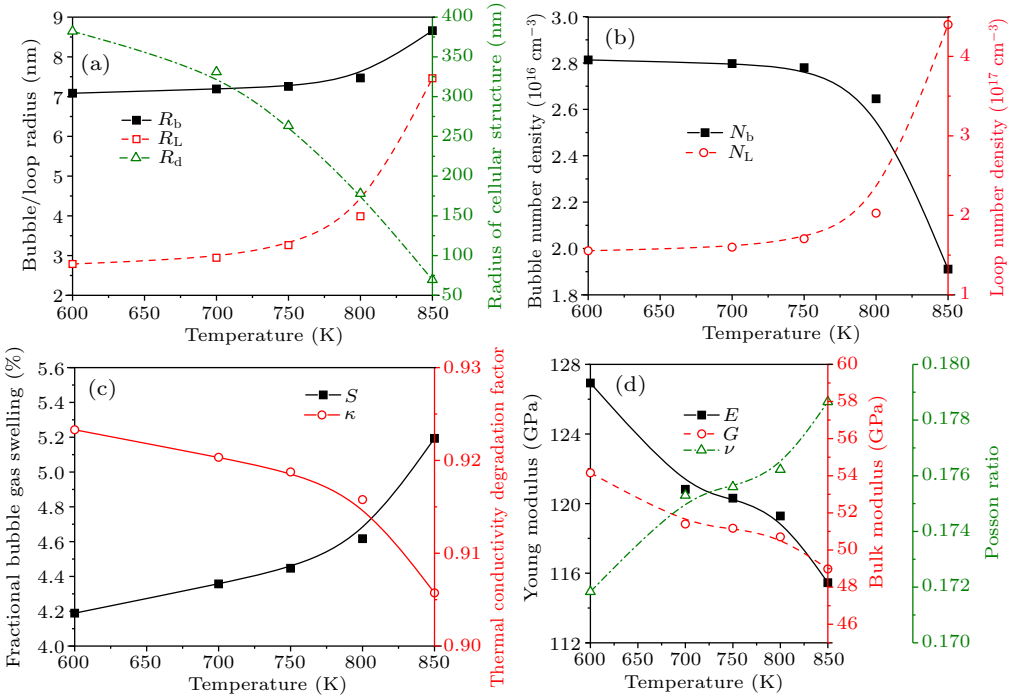


Fig. 3. Temperature dependencies of bubble, loop, and dislocation cell radii (a), bubble and loop number densities (b), swelling and thermal conductivity degradation factor (c), elastic moduli and Poisson ratio (d) at fixed fission density $F_d = 3 \times 10^{21}$ cm^{-3} at fission rate $\dot{f} = 2.5 \times 10^{14}$ (cm^3·s)$^{-1}$.

From Fig. 3(b), it is evident that the rapid decrease in N_b with temperature correlates well with the increase in bubble size and the temperature-driven effect of bubble coalescence. Simultaneously, the rapid increase in loop number density is primarily associated with enhanced defect clustering at elevated temperatures.

Using the obtained data for R_b and N_b, we calculate the temperature dependencies of both swelling and the thermal conductivity degradation factor, as shown in Fig. 3(c). Swelling increases with temperature due to bubble size growth, ranging from 4.2% to 5.4% over the temperature interval 600 K to 850 K. The thermal conductivity degradation factor decreases with increasing temperature, consistent with the results reported in Ref. [17], and remains within the same range of values.

It should be noted that the magnitudes of bubble size, number density, and swelling at the selected fission density agree well with the results discussed in Ref. [19] for the same irradiation time and with data from Ref. [15]. The variation of elastic moduli and Poisson ratio with temperature is shown in Fig. 3(d). A pronounced decrease in both Young's modulus and shear modulus is observed at elevated temperatures, coinciding with a sharp increase in porosity. The Poisson ratio, defined as $\nu = E/(2G) - 1$, exhibits a slight increase with temperature.

3.3. Flux effect

To investigate the effect of flux, the temperature is fixed while the fission rate is varied. Typical protocols at different fission rates are shown in Fig. 4.

From the obtained dependencies, one can conclude that the bubble size attains lower values at the same fission densities. A noticeable difference in bubble size is observed only at elevated fission densities, as illustrated by the inset in Fig. 4(a). This behavior is attributed to the increased resolution rate, which is proportional to the fission rate. Comparing the dependencies of loop radius and the radius of the cellular dislocation structure reveals a similar effect for the loop radius, whereas a slight increase in the dislocation cell size is observed only at high fission density (see Fig. 4(b)).

The obtained protocols were used to determine values for the measured quantities. The most significant changes in these quantities are observed at elevated fission densities. To illustrate the flux effects, the main trends at $F_d = 10^{22}$ cm^{-3} are presented in Fig. 5.

From Fig. 5(a), it follows that the mean bubble radius decreases with increasing fission rate, whereas the loop radius increases due to the large production of interstitials. The size of the dislocation cell structure decreases, indicating an increase in the network dislocation density. The dependencies of both bubble and loop number densities, shown in Fig. 5(b), exhibit an increasing trend with fission rate. Meanwhile, swelling in Fig. 5(c) shows a decreasing trend due to the competing effects of bubble size and number density. The computed thermal conductivity degradation factor increases with fission rate. Dependencies of the elastic moduli *versus* fission rate exhibit an increasing trend due to the reduction in swelling, while the Poisson ratio decreases with increasing fission rate.

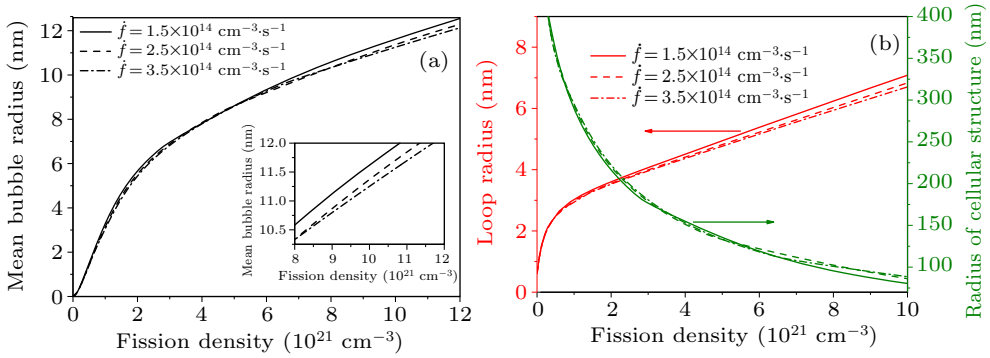


Fig. 4. Typical protocols for mean bubble radius (a), dislocation loop and dislocation cell structure (b) at different fission rate and temperature 800 K.

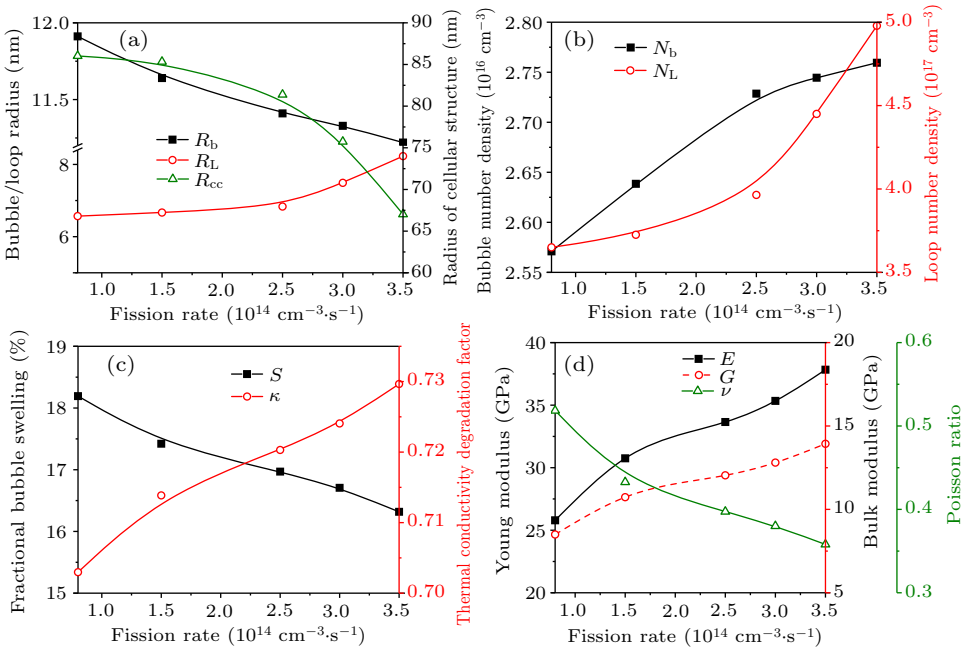


Fig. 5. Fission rate dependencies of bubble, loop, and dislocation cell radii (a), bubble and loop number densities (b), swelling with thermal conductivity degradation factor (c), elastic moduli and Poisson ratio (d) at fixed fission density $F_d = 10\times10^{21}$ cm^{-3} and temperature $T = 800$ K.

3.4. Distribution function over bubble size and scaling dynamics

To consider the bubble size distribution under different irradiation regimes, one must derive a mathematical expression for the bubble size distribution function $\Phi(R_b)$. To this end, we follow the approach described in Ref. [23], neglecting bubble diffusion and assuming that the resolution volume b_0 is constant.

Let $\Phi(R_b)\mathrm{d}R_b$ represent the number of bubbles per unit volume with radii between R_b and $R_b+\mathrm{d}R_b$. The growth and resolution of bubbles due to irradiation are described by

$$\left[\frac{\mathrm{d}\Phi}{\mathrm{d}t}\right]_g \mathrm{d}R_b = -\frac{\mathrm{d}}{\mathrm{d}R_b}\left[\Phi(R_b)\frac{\mathrm{d}R_b}{\mathrm{d}t}\right]\mathrm{d}R_b,$$
$$\left[\frac{\mathrm{d}\Phi}{\mathrm{d}t}\right]_r = -b_0\dot{f}\Phi(R_b). \tag{8}$$

The total rate is then given by

$$\left[\frac{\mathrm{d}\Phi}{\mathrm{d}t}\right]_{tot} = \left[\frac{\mathrm{d}\Phi}{\mathrm{d}t}\right]_g + \left[\frac{\mathrm{d}\Phi}{\mathrm{d}t}\right]_r. \tag{9}$$

An equilibrium bubble population is defined in the stationary case by

$$\frac{\mathrm{d}\Phi(R_b)}{\mathrm{d}R_b}v(R_b) + \Phi(R_b)\frac{\mathrm{d}v(R_b)}{\mathrm{d}R_b} + b_0\dot{f}\Phi(R_b) = 0, \tag{10}$$

where the bubble growth speed

$$v(R_b) = \frac{1}{4\pi R_b^2}\left(\Omega_g\frac{\mathrm{d}m_b}{\mathrm{d}t} + \Omega_v\frac{\mathrm{d}n_{vb}}{\mathrm{d}t}\right) \tag{11}$$

is defined from the bubble volume $V_b = 4\pi R_b^3/3$.

The solution of the equation for the distribution function can be expressed in quadratures as

$$\Phi(R_b) = \frac{C_0}{v(R_b)}\exp\left(-b_0\dot{f}\int_{R_b}\frac{\mathrm{d}R}{v(R)}\right). \tag{12}$$

A non-stationary solution of the equation for the distribution function $\Phi(R_b,t)$ can be found in the self-similar (automodel) regime. To this end, we apply the Fourier method and write

$$\Phi(R_b,t) = \phi(t)\rho(y), \quad y = \frac{R_b(t)}{a(t)}, \tag{13}$$

where y is the bubble radius scaled by $a(t)$, and $\phi(t)$ and $\rho(y)$ are unknown functions. The time derivative of the bubble radius defines the bubble growth speed $\mathrm{d}R_\mathrm{b}/\mathrm{d}t = \theta(t)\omega(y)$, where the time dependence defined by $\theta(t)$ should coincide with $\dot{a}(t)$, consistent with the definition of the bubble size derivative, i.e., $\theta(t) \equiv \dot{a}(t)$.

By taking time and spatial derivatives in Eq. (9), we arrive at the equation

$$\frac{a(t)}{\dot{a}(t)}\left(\frac{\dot{\phi}(t)}{\phi(t)} + b_0\dot{f}\right) = \frac{1}{\rho(y)}\frac{\mathrm{d}}{\mathrm{d}y}\omega(y)\rho(y). \tag{14}$$

Separating variables for t and y, we obtain the following solutions:

$$\begin{aligned}
&\phi(t) = \phi_0[a(t)]^{-C}\exp(-b_0\dot{f}t/\tau_\phi),\\
&\rho(y) = \frac{\rho_0}{\omega(y)}\exp\left(-C\int^y\frac{\mathrm{d}y'}{\omega(y')}\right),
\end{aligned} \tag{15}$$

where ϕ_0, τ_ϕ, and ρ_0 are integration constants and $C > 0$.

Consequently, one obtains

$$\begin{aligned}
&N_\mathrm{b}(t) = N_0[a(t)]^{1-C}\exp(-b_0\dot{f}t/\tau_\phi),\\
&N_0 = \phi_0\int_0^\infty\rho(y)\mathrm{d}y,\\
&\langle R_\mathrm{b}(t)\rangle = \langle R_{\mathrm{b}0}\rangle a(t),\\
&\langle R_{\mathrm{b}0}\rangle = \frac{\int_0^\infty y\rho(y)\mathrm{d}y}{\int_0^\infty\rho(y)\mathrm{d}y}, \quad a(t)\propto t^z.
\end{aligned} \tag{16}$$

Using experimental data for the exponential decay of the bubble number density at elevated fission density, where bubble coalescence dominates bubble evolution (see Ref. [23]), one can set $C = 1$. This leads to $N(t) \propto \exp(-t/\tau_\mathrm{N})$, where $\tau_\mathrm{N} = \tau_\phi/(b_0\dot{f})$, and τ_ϕ is determined by fitting the experimental data.

From the obtained solution, it follows that the bubble size distribution function exhibits universal behavior independent of the time scale. Moreover, the bubble size scale $a(t) \propto t^z$ (where z relates to the Hölder exponent, $z \in [0, 1]$) follows a power-law dependence characteristic of the coalescence regime. This scaling describes the self-similar dynamics of the system and its universal properties, where all measured quantities can be scaled through the bubble size time scale $a(t)$.

By considering that the swelling follows a general power-law dependence $s_\mathrm{b} \propto (\dot{f}t)^s$, one can deduce that $\langle R(t)\rangle \propto (\dot{f}t)^{s/3}$, where the exponent s characterizes different dominant mechanisms governing swelling: for vacancy voids, $s = 1$, whereas for purely gas bubbles, $s = 3/2$.[23] By analyzing changes in the slope $z = s/3$ in a log–log plot of bubble size versus time, one can identify the dominant mechanism in bubble growth dynamics. Generally, even in amorphous systems where only gas atoms are considered, the exponent s varies at different stages of bubble growth.[35]

Using protocols for bubble size, one can determine $v(R_\mathrm{b})$ and perform numerical integration to obtain normalized bubble size distribution functions, as shown in Fig. 6(a) for different temperatures and fission rates. It is found that the distribution function $\Phi(R_\mathrm{b})$ follows a log-normal fit regardless of the irradiation conditions. On the other hand, increasing temperature leads to a heavier tail of the distribution at larger bubble sizes; correspondingly, the distribution peak decreases and shifts toward larger bubble sizes. Conversely, decreasing the fission rate results in an increased peak for the most probable bubble radius, while the tail of the distribution becomes confined to a narrower range of bubble sizes.

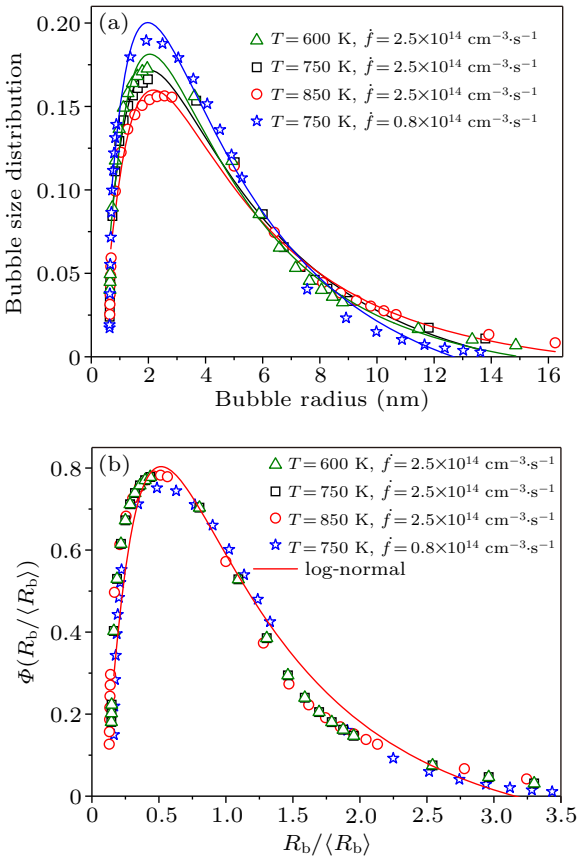


Fig. 6. Bubble size distribution functions at different temperatures and fission rates: (a) $\Phi(R_\mathrm{b})$, (b) universal distributions $\Psi(R_\mathrm{b}/\langle R_\mathrm{b}\rangle)$.

To demonstrate the universality of the bubble size distribution, we compute the distribution function $\Psi(R_\mathrm{b}/\langle R_\mathrm{b}\rangle)$, where the statistical average is defined as $\langle R_\mathrm{b}\rangle = \int R_\mathrm{b}\Phi(R_\mathrm{b})\mathrm{d}R_\mathrm{b}$. The corresponding dependencies of $\Psi(R_\mathrm{b}/\langle R_\mathrm{b}\rangle)$ under identical irradiation conditions are shown in Fig. 6(b). It is clearly observed that all the obtained data collapse onto a single universal fit, for which we employ a log-normal fitting procedure. This indicates that the distribution function $\Psi(R_\mathrm{b}/\langle R_\mathrm{b}\rangle)$ exhibits universal behavior, i.e., it is independent of irradiation conditions and time scales.

Next, we analyze the scaling laws for bubble size growth. The dependencies $R_\mathrm{b}(F_\mathrm{d})$ at different temperatures, plotted on a double logarithmic scale, are shown in Fig. 7(a). Here,

empty markers correspond to fission density values at which the condition $m_b/n_{vb} = 1$ holds. It is found that at fission densities where $m_b/n_{vb} \gg 1$, the scaling exponent s in the relation $R_b(\dot{f}t) \propto t^{s/3}$ is larger than in the regime where $m_b/n_{vb} \ll 1$. Using the scaling exponent $z = s/3$ in the first regime, one obtains $z = 0.62$ with $s = 1.86$, which is close to the theoretical value of $3/2$ corresponding to gas atom-controlled bubble growth. In this regime, bubbles consist predominantly of gas atoms. In the second regime, one finds $z = 0.37$ and $s = 1.11$, which is close to the theoretical value of $s = 1$, where bubbles are primarily vacancy-dominated. This implies that in the intermediate regime, the competing growth mechanisms act simultaneously. The value of the scaling exponent z (or s) shows minimal dependence on irradiation conditions.

In Fig. 7(b), we plot the bubble growth rate $v(F_d)$ to illustrate that growth driven by gas atoms dominates during the initial stage when bubbles are sufficiently small, while vacancy-driven growth becomes significant for larger bubbles where resolution effects are pronounced. Here black lines relate to $\partial_t m_b$, red lines correspond to $\partial_t n_{vb}$.

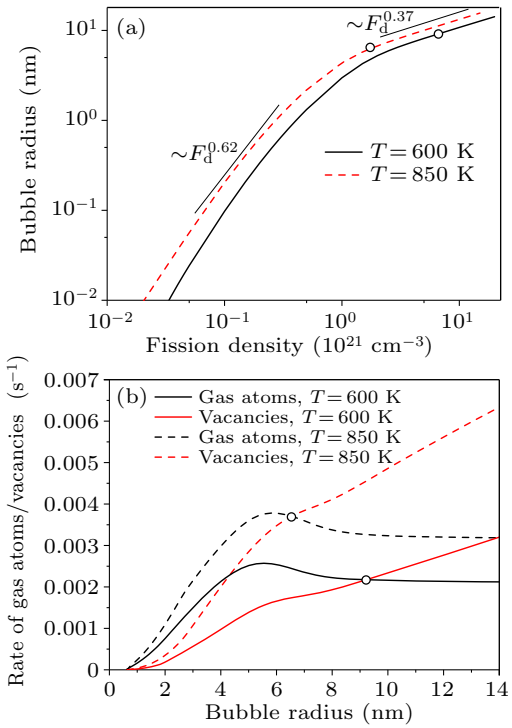


Fig. 7. Crossover of dynamical regimes of bubble growth at $\dot{f} = 2.5 \times 10^{14}$ (cm^3·s)$^{-1}$: (a) log–log plots of bubble radius protocols at different temperatures, (b) bubble growth rates by gas atoms ($\partial_t m_b$) and vacancy ($\partial_t n_{vb}$) mechanisms. Empty markers correspond to the case $m_b/n_{vb} = 1$.

It follows that, at both low and high temperatures, bubble growth is governed by the interplay of both competing mechanisms. Specifically, the growth of small bubbles is predominantly controlled by gas atoms at low temperatures, whereas at high temperatures, small bubble growth is influenced by both mechanisms. At high fission densities, the majority of bubble growth is driven by the increasing rate associated with vacancies. As the temperature rises, the corresponding fission density at which the ratio $m_b/n_{vb} = 1$ holds decreases compared to that at lower temperatures. Since both mechanisms contribute to the growth dynamics, this explains the observed differences in scaling exponents, which tend to be higher than the theoretical values. Moreover, the actual scaling behavior is more complex than the simple algebraic law typically employed.

4. Conclusions

We propose a generalized model based on the reaction rate theory formalism for fission gas bubble growth to describe the dynamics of an ensemble of bubbles in crystalline systems with evolving defect microstructure. The developed formalism is grounded in experimental observations of gas atom accumulation at multiple types of sinks, such as dislocations and grain boundaries,[20] as well as in the development of cellular dislocation structures that limit the growth of dislocation loops and influence bubble growth dynamics.[18,21,22] It was demonstrated that bubble growth within cellular dislocation structures formed by network dislocations and dislocation loops is controlled by two competing mechanisms related to the accumulation of gas atoms and vacancies.

It was shown that with increasing temperature, the sizes of both bubbles and dislocation loops increase, whereas the size of the cellular dislocation structure decreases. Simultaneously, the number density of bubbles decreases with temperature, while the density of dislocation loops increases. The temperature-dependent growth of swelling and the corresponding decrease of the thermal conductivity degradation factor were examined. Elastic moduli were found to decrease with increasing temperature.

Bubble size and loop size exhibit opposite trends with increasing fission rate: bubble size decreases while loop size increases; concurrently, the cellular structure size decreases with fission rate. The number densities of both bubbles and loops increase with fission rate. Swelling exhibits a decaying dependence on fission rate, opposite to the behavior of the thermal conductivity degradation factor. The increase in elastic moduli with fission rate correlates well with the decrease in swelling. The flux effect studied here is most pronounced at elevated fission densities.

Scaling and universal properties of bubble growth were investigated under different irradiation regimes. It was found that at the initial stages of bubble growth, when bubble sizes are up to several nanometers, the dominant contribution to growth is governed by gas atoms. The corresponding asymptotic behavior, $R_b(t) \propto t^z$, follows approximately a parabolic law with the scaling exponent $z \simeq 1/2$. For larger bubbles, vacancy-mediated mechanisms dominate. Accumulation of vacancies in bubbles with radii around 10 nm slows their

growth, resulting in a crossover to a sub-parabolic regime characterized by a scaling exponent $z \simeq 1/3$. The relative contributions of these processes are governed by the ratio of gas atoms to vacancies within a bubble. This crossover regime is observed over typical ranges of temperature and fission rate, with scaling exponents z only weakly dependent on irradiation conditions. The relative bubble size distribution exhibits a universal character, independent of irradiation conditions.

The obtained results for bubble size, number density, dislocation cellular structure size, swelling, and the corresponding degradation factor values correspond well with existing experimental and theoretical/numerical findings reported in Refs. [15–17,19,23] under comparable irradiation temperature and fission rate conditions. Accordingly, the authors anticipate that the developed model and results can be applied to further studies of material behavior (specifically U_3Si_2) under different irradiation regimes by a coupled consideration of gas bubbles and evolving defect structures.

Acknowledgements

Project supported by the Fund from Sichuan Science and Technology Program (Grant No. 2024JDHJ0014), the Joint Funds of the National Natural Science Foundation in China (Grant No. U23B2071), and the Fund from the Ministry of Education and Science of Ukraine (Grant No. 0124U000551).

References

[1] Leenaers A, Wight J, Van den Berghe S, Ryu H J and Valery J F 2020 U-Si-based fuel system *Comprehensive Nuclear Materials: Second Edition* (Elsevier) pp. 485–498
[2] Terrani K A, Wang D, Ott L J and Montgomery R O 2014 *J. Nucl. Mater.* **448** 512
[3] Berche A, Rado C, Rapaud O, Guéneau C and Rogez J 2009 *J. Nucl. Mater.* **389** 101
[4] Mohamad A, Ohishi Y, Muta H, Kurosaki K and Yamanaka S 2018 *J. Nucl. Sci. Technol.* **55** 1141
[5] Gamble K A, Pastore G, Cooper M W D and Andersson D 2019 *ATF material model development and validation for priority fuel concepts Tech. Rep. Idaho National Lab. (INL)*, Idaho Falls, ID (United States)
[6] Sun D, Yang Q, Zhao J, Gao S, Xin Y, Zhou Y, Yin C, Chen P, Zhao J and Wang Y 2024 *Chin. Phys. B* **33** 016105
[7] Shimizu H 1965 *The properties and irradiation behavior of* U_3Si_2 (Atomics International)
[8] Hofman G L 1986 *J. Nucl. Mater.* **140** 256
[9] Finlay M, Hofman G and Snelgrove J 2004 *J. Nucl. Mater.* **325** 118
[10] Leenaers A, Koonen E, Parthoens Y, Lemoine P and Van den Berghe S 2008 *J. Nucl. Mater.* **375** 243
[11] Kim Y S, Hofman G, Rest J and Robinson A 2009 *J. Nucl. Mater.* **389** 443
[12] Winter T and Deo C 2017 *Annals of Nuclear Energy* **100** 31
[13] Miao Y, Gamble K A, Andersson D, Mei Z G and Yacout A M 2018 *Nuclear Engineering and Design* **326** 371
[14] Williamson R L, Hales J, Novascone S, Tonks M, Gaston D, Permann C, Andrs D and Martineau R 2012 *J. Nucl. Mater.* **423** 149
[15] Miao Y, Gamble K A, Andersson D, Ye B, Mei Z G, Hofman G and Yacout A M 2017 *Nuclear Engineering and Design* **322** 336
[16] Miao Y, Ye B, Hofman G, Yacout A, Gamble K and Mei Z G 2016 *Rate theory modeling and simulation of silicide fuel at lwr conditions Tech. rep. Argonne National Lab. (ANL)*, Argonne, IL (United States)
[17] Tonks M R, Liu X Y, Andersson D, Perez D, Chernatynskiy A, Pastore G, Stanek C R and Williamson R 2016 *J. Nucl. Mater.* **469** 89
[18] Rest J 2006 *J. Nucl. Mater.* **349** 150
[19] Barani T, Pastore G, Pizzocri D, Andersson D, Matthews C, Alfonsi A, Gamble K, Van Uffelen P, Luzzi L and Hales J 2019 *J. Nucl. Mater.* **522** 97
[20] Miao Y, Harp J, Mo K, Zhu S, Yao T, Lian J and Yacout A M 2017 *J. Nucl. Mater.* **495** 146
[21] Rest J and Hofman G 1994 *J. Nucl. Mater.* **210** 187
[22] Rest J and Hofman G 2000 *J. Nucl. Mater.* **277** 231
[23] Rest J 2004 *J. Nucl. Mater.* **325** 107
[24] Aagesen L K, Andersson D, Beeler B W, Cooper M W, Gamble K A, Miao Y, Pastore G and Tonks M R 2020 *J. Nucl. Mater.* **541** 152415
[25] Hu S, Setyawan W, Beeler B W, Gan J and Burkes D E 2020 *J. Nucl. Mater.* **542** 152441
[26] Golubov S, Barashev A and Stoller R 2012 *Comprehensive Nuclear Materials* **1** 357
[27] Singh B, Golubov S, Trinkaus H, Serra A, Osetsky Y N and Barashev A 1997 *J. Nucl. Mater.* **251** 107
[28] Marquez M G, Ougouag A M and Petrovic B 2020 *Annals of Nuclear Energy* **145** 105712
[29] Wang Y, Xiao Z, Hu S, Li Y and Shi S Q 2020 *Comput. Mater. Sci.* **183** 109817
[30] Olander D R 1976 *Fundamental aspects of nuclear reactor fuel elements: solutions to problems Tech. rep. California Univ., Berkeley (USA)* Dept. of Nuclear Engineering
[31] Hastings J, MacEwan J and Bourque L 1972 *J. Am. Ceram. Soc.* **55** 240
[32] Remschnig K, Le Bihan T, Noël H and Rogl P 1992 *J. Solid State Chem.* **97** 391
[33] Kogai T 1997 *J. Nucl. Mater.* **244** 131
[34] Bender O and Ehrhart P 1983 *J. Phys. F: Metal Phys.* **13** 911
[35] Kharchenko D O, Kharchenko V O, Shchokotova O M and Wu L 2023 *Philosophical Magazine* **103** 1311